



Study on the formability and texture evolution of AA6061 alloy processed by repetitive corrugation and straightening

S. Elizalde^a • M. Ezequiel^b • J. M. Cabrera^{a,c} • I. A. Figueroa^b •
M. Teresa Baile^d • G. Gonzalez^{b*}

^aDepartamento de Ciencia e Ingeniería de Materiales, EEBE - Universidad Politécnica de Cataluña, Barcelona, Spain

^bInstituto de Investigaciones en Materiales, Universidad Nacional Autónoma de México, Ciudad de México, Mexico

^cInstituto de Investigaciones Metalúrgicas y Materiales, Universidad Michoacana de San Nicolás de Hidalgo, Morelia, Michoacan, Mexico

^dDepartamento de Ciencia e Ingeniería de Materiales, CDAL - Universidad Politécnica de Cataluña, Vilanova i la Geltrú Spain

Received 05 03 2021; accepted 07 02 2021

Available 10 31 2021

Abstract: The severe plastic deformation (SPD) techniques allow obtaining ultrafine-grained materials. Different SPD techniques permit processing sheet shape materials such as repetitive corrugation and straightening (RCS) and accumulative roll bonding (ARB). In this study, the formability of an AA 6061-T6 processed by RCS was evaluated. The forming limit diagrams (FLD) were obtained by Nakazima tests after one and two RCS cycles. The FLD curves showed that the forming capacity decreased from the first RCS cycle. Likewise, uniaxial tensile tests at different temperatures and strain rates were conducted to analyze the effect of the RCS process on the strain rate sensitivity. They showed a relatively high strain rate sensitivity coefficient in the samples after one and two RCS cycles. Finally, the initial texture showed a predominant cube texture component, whereas, for further RCS cycles, a weakening of the cube texture and an increment of the S texture component were observed.

Keywords: Aluminum alloys, RCS, forming capacity, crystal texture, SPD

*Corresponding author.

E-mail address: josegr@unam.mx (G. Gonzalez).

Peer Review under the responsibility of Universidad Nacional Autónoma de México.

1. Introduction

The 6xxx series of aluminum alloys are good candidates to replace some steels in the automotive industry because of their excellent mechanical properties, low density, corrosion resistance, and recyclability. Even though having a high strength-to-weight ratio, the use of aluminum alloys is limited due to their relatively low formability and large spring back at room temperature compared to traditional steel sheets (Chen et al., 2017; Miller et al., 2000).

On the other hand, the enhanced mechanical properties in different aluminum alloys obtained by refining the grain size down to the ultrafine-grained (UFG) regime have received considerable attention in recent years. In this sense, severe plastic deformation (SPD) techniques allow for processing metallic materials to generate UFG materials. Several SPD processes such as equal channel angular pressing (ECAP), equal channel angular rolling (ECAR), high-pressure torsion (HPT), accumulative roll bonding (ARB), repetitive corrugation and straightening (RCS), and constrained groove pressing (CGP) have been developed (Bozcheloei et al., 2019; Huang et al., 2004; Shin et al., 2002; Valiev et al., 2000; Yu et al., 2016). Particularly ECAR, ARB, CGP, and RCS are specially designed to produce sheet-shape UFG materials. A characteristic feature of the SPD processes is that the shape and dimensions remain almost constant, i.e., the process mostly generates semi-finished parts. Hence, the UFG products usually require further shaping steps, like cutting or extra forming processes. Indeed, one of the factors responsible for the slow commercialization progress of the SPD processed materials is the lack of knowledge regarding the post-SPD shaping (Azushima et al., 2008; Bruder, 2019).

It is well known that formability depends on external and internal factors; therefore, there is not a universal parameter to measure such property (Bruder, 2019). Usually, the literature regarding SPD processes emphasizes the enhancement of mechanical properties based on the uniaxial tensile or hardness tests (Entezami et al., 2016; Roy et al., 2012; Shin et al., 2002). The applicability of the parameters obtained by a uniaxial tensile test into the formability measurement, such as the uniform elongation and the elongation to failure, is debatable. Despite that uniaxial tension rarely occurs in a forming operation, the uniform elongation is taken as a good indicator of the onset of strain localization (i.e., necking). However, biaxial stress states mainly occur in the most common forming operations like deep drawing, stretch drawing, and bending (Bruder, 2019).

Nevertheless, formability can be described in different ways, being the forming limit diagram (FLD), one of the most employed. These diagrams are defined in the principal strain space (ϵ_1 - ϵ_2) where safe strain combinations are separated from the fracture or necking condition (Ravishankar &

Venkadesan, 1996). For characterizing a wide area of the principal strain space, different strain combinations can be obtained by changing the shape of the tested samples, which allow covering from the uniaxial tension to equi-biaxial tension states range.

Few publications have been reported the FLDs of SPD processed materials. Rahimi et al. (2018) studied the formability of the Al 5083 aluminum alloy processed by ECAR (with an intersecting angle of 130°) up to 3 passes at room temperature. They found that the major strain forming limit at plane strain condition (FLD₀) decreased by increasing the number of ECAR passes. In further studies, Bozcheloei et al. (2019) reported the temperature effect (room temperature, 473 K, and 573 K) during the ECAR process on the formability of the same alloy with an ECAR die with the same configuration mentioned above. Their results showed that the FLD₀ still decreased for the higher processed sample temperatures. Similarly, Ezequiel et al. (2020) showed that the FLD₀ and biaxial ductility of Al 5754 aluminum alloy processed by RCS decreased after one pass, while a significant loss of the forming capacity was observed after two RCS passes. Lapovok et al. (2008) studied the formability of the Al-6111 alloy processed at room temperature by ECAP up to 2 passes. The analysis of the forming behavior showed a substantial drop in the biaxial ductility and FLD₀ after the first pass, while for the second pass, no further diminution of the biaxial ductility was observed, but a recovery of the FLD₀ value. Rahmatabadi and Hashemi (2017) obtained similar results showing the formability evolution of an Al 1050 alloy after the ARB process. A considerable decrease in FLD₀ was also observed in the ARB cycle compared with the annealed condition. For further passes, FLD₀ increased with every subsequent cycle but remained below the annealed condition.

One of the possible solutions to improve the formability of aluminum alloys is to increase the forming temperature. Under these conditions, the strain rate sensitivity parameter at each temperature becomes a key indicator of the forming capacity. This parameter can be interpreted as the ability of the material to keep the homogeneous deformation and delay fracture as a function of the strain rate applied (Chen et al., 2017; Ezequiel et al., 2020). Moreover, the grain size also has a considerable effect during the hot forming processes, especially when the grain size is fine enough (usually below 10 μm) to promote superplastic behavior, which in turn allows extraordinarily large homogeneous elongations (Khamei & Dehghani, 2015). There are few studies on UFG materials obtained by SPD processes, especially on the Al 6061 and their effect on the hot deformation. Khamei and Dehghani (2015) studied the effects of two combined SPD processes (ECAP + cold rolling) on some thermomechanical parameters (strain rate sensitivity, hot ductility, etc.). They found that the microstructural refinement leads to a higher elongation to

failure when compared to the undeformed condition. The maximum strain rate sensitivity ($m=0.23$) was observed at 573 K; this value decreased at higher temperatures.

Finally, the crystallographic texture also influences the forming behavior. In aluminum alloys, the texture typically develops around copper $\{112\} < 11\bar{1} >$, brass $\{110\} < 1\bar{1}2 >$, and S $\{123\} < 63\bar{4} >$ orientations during the rolling process, and around cube $\{001\} < 100 >$ and Goss $\{110\} < 001 >$ orientations during the annealing process [18, 19]. Some authors have reported that the Cube texture component is beneficial for formability (Barlat & Richmond, 1987; Yoshida et al., 2007), while some other authors have reported that it is detrimental (Ratchev et al., 1994; Sakai et al., 2001). Therefore, to correlate the effect of the crystallographic texture on the formability, a systematic study of the texture components, complemented with some mechanical characterization, is highly pertinent. Thus, the objective of the present work is to study the formability evolution and crystallographic texture of Al-6061-T6 sheets processed by RCS up to two cycles. A systematic macrotexture analysis obtained by X-ray diffraction (XRD) was also assessed.

2. Methodology

The starting material was a commercial Al-6061 sheet of 0.9 mm in thickness. The chemical composition obtained by X-ray fluorescence is shown in table 1. The Al-6061 is mainly used in T6 conditions due to the relatively higher mechanical performance when compared to other conditions. For obtaining this condition, all elements were put in solid solution by soaking at 803.15 K for two hours, and then the samples were water quenched. After that, an aging treatment was carried out at 453.15 K for 18 h.

Once the material was in the T6 condition, Al-6061 sheets were cut with dimensions of 120 x 120 x 0.9 mm and then processed by RCS up to two cycles. The RCS process consists of repetitive pressing a thin metal sheet between two grooved dies to generate high shear strain on the deformed sample (see Fig. 1a). Later the same process is repeated with two flat dies to recover the initial shape of the sample. In the present study, one RCS cycle is defined as one corrugation step followed by a strengthening one, then rotated 90° along the normal direction (ND) in order to alternate the deformation zone, and finally, another corrugation and straightening steps are impaired. The RCS sinusoidal profile of the die with an amplitude of 2 mm and a period of 16 mm is shown in Fig. 1b. More details of the process can be found elsewhere (Elizalde et al., 2020).

The FLDs were obtained for samples at the T6 aged condition and with one and two RCS cycles using the Nakazima test at room temperature. For these tests, a hemispherical

punch with a diameter of 50 mm was used. The punch velocity was set as 1 mm s⁻¹ and stopped when the load sensor detected a sudden drop (i.e., the onset of fracture), and a configuration of Teflon-PVC-Teflon was used as a lubrication system. The standard ISO 12004-2:2008 was followed to define sample geometries and experimental procedures. Five different geometries were machined to obtain different strain paths (shaft parallel to rolling direction), from biaxial to uniaxial tension (Fig. 2), including the plane strain condition. Three samples for each geometry were tested to have experimental repeatability. Samples were coated with white paint, and then black speckles were sprayed for image analysis purposes. The strain was measured by a digital image correlation (DIC) system and analyzed by the ARAMIS® software, using the three sections method.

Uniaxial tensile tests at different temperatures and strain rates were conducted to analyze the effect of the RCS process on the strain rate sensitivity. The sample geometries were based on the ASTM E8M standard with a gauge length of 50 mm (Fig. 3). The tensile tests were performed on samples after one and two RCS cycles. A universal testing machine, INSTRON 5584, equipped with a cylindrical furnace, was employed for this purpose. The tensile test temperatures were set as 573, 673, and 773 K; and three different strain rates were used for each temperature, i.e., $3 \times 10^{-5} \text{ s}^{-1}$, $3 \times 10^{-4} \text{ s}^{-1}$, and $3 \times 10^{-3} \text{ s}^{-1}$.

The strain rate sensitivity coefficient “m” was calculated according to equation (1):

$$\sigma = C \dot{\epsilon}^m \quad (1)$$

where σ is the stress, C is a material constant and $\dot{\epsilon}$ corresponds to strain rate. Two specimens were tested for each combination of temperature and strain rate. The maximum values obtained for the tensile stress, with their corresponding strain rate, were plotted in a logarithmic scale, and a linear fit of the data was carried out. The slope of the plot corresponds to the strain rate sensitivity coefficient “m”.

The crystallographic texture was measured with a diffractometer Rigaku Ultima IV, with a wavelength of Cu-K α . The configuration was set on “in-plane” mode, with an angle range α from 0.5 to 90° and β from 0 to 360°. The specimens were metallographically prepared to mirror finishing before measurements. The sample reference configuration is shown in Fig. 4. For representing the crystallographic orientation on the Euler’s space, the orientation distribution functions (ODFs) are usually employed. The ODFs were calculated from the experimentally obtained pole figures (111), (200), and (220) using the software MATLAB® toolbox MTEX for samples in the initial condition and after one and two RCS cycles.

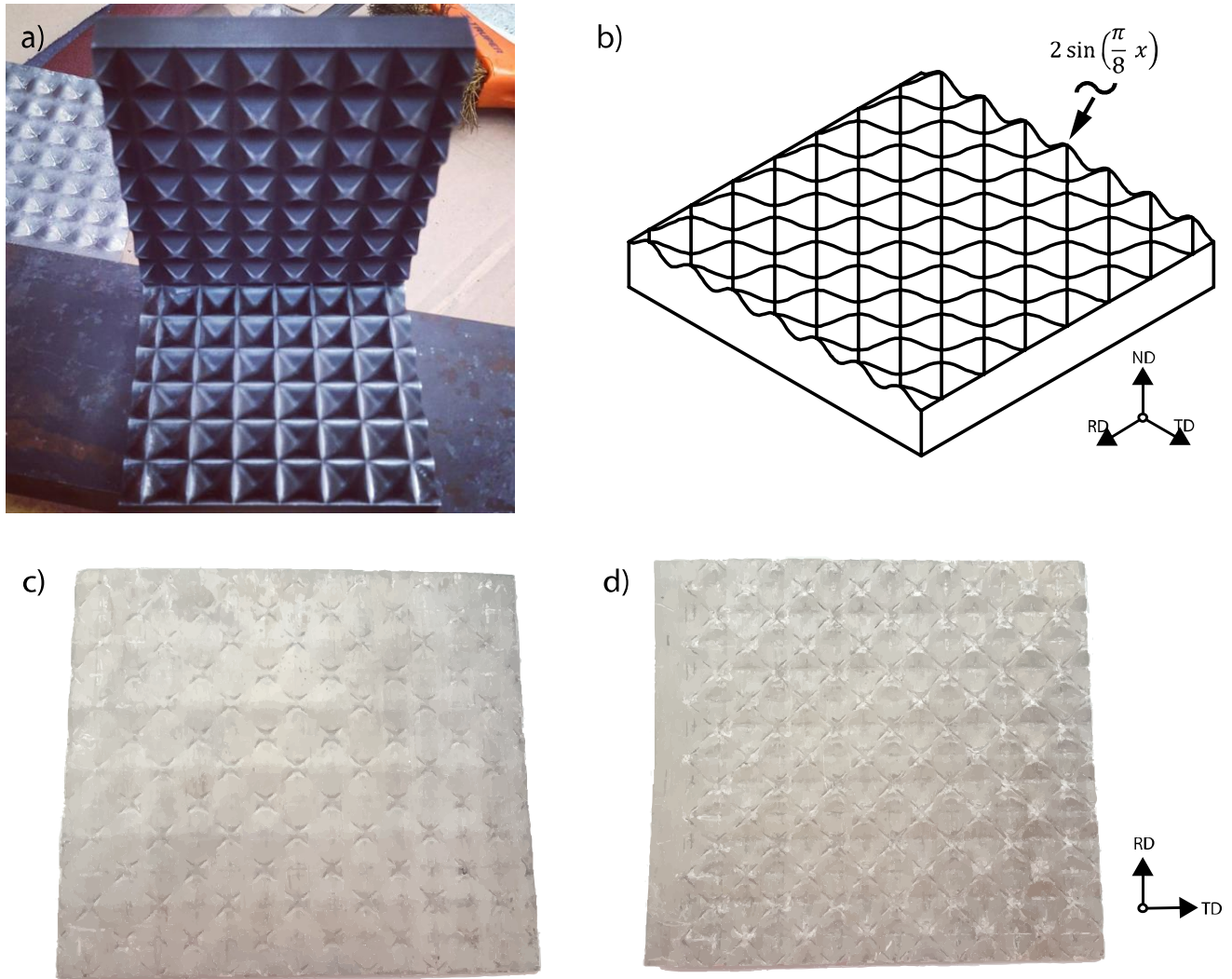


Figure 1. a) Repetitive corrugation and straightening die made of D2 steel, b) sinusoidal profile, used for the die design, with an amplitude of 2 mm and a period of 16 mm, c) 1C RCS processed sample and d) 2C RCS processed sample.

Table 1. Composition of the studied Al-6061 alloy.

Element	Si	Fe	Cu	Mn	Mg	Cr	Zi	Ti	Al
%wt	0.77	0.24	0.16	0.03	1.03	0.07	0.07	0.02	Balance

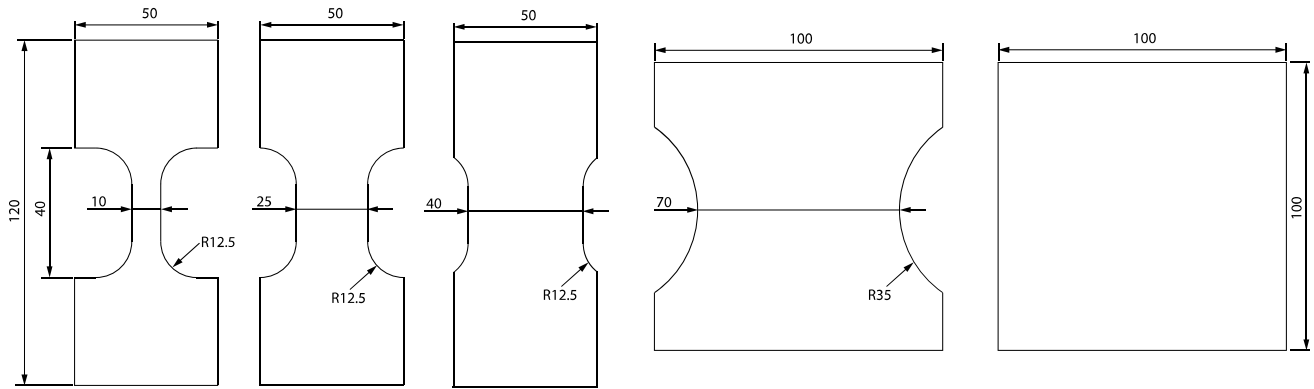


Figure 2. Geometries of the samples used for the Nakazima test (dimensions in mm)

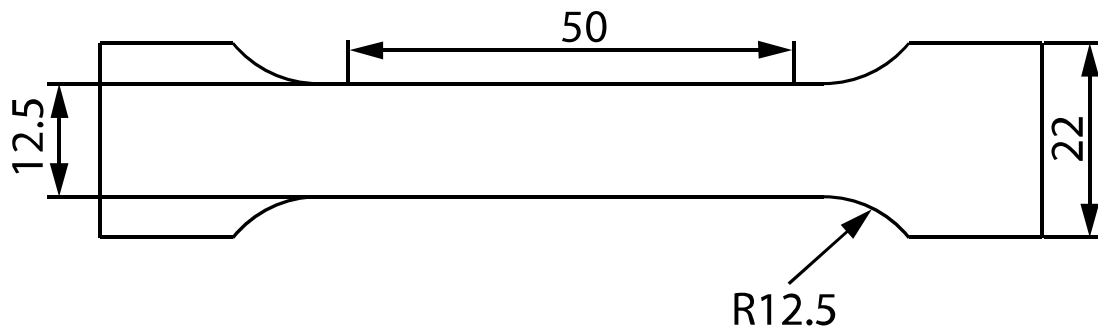


Figure 3. Dimensions (in mm) of the sample employed for the hot tensile test.

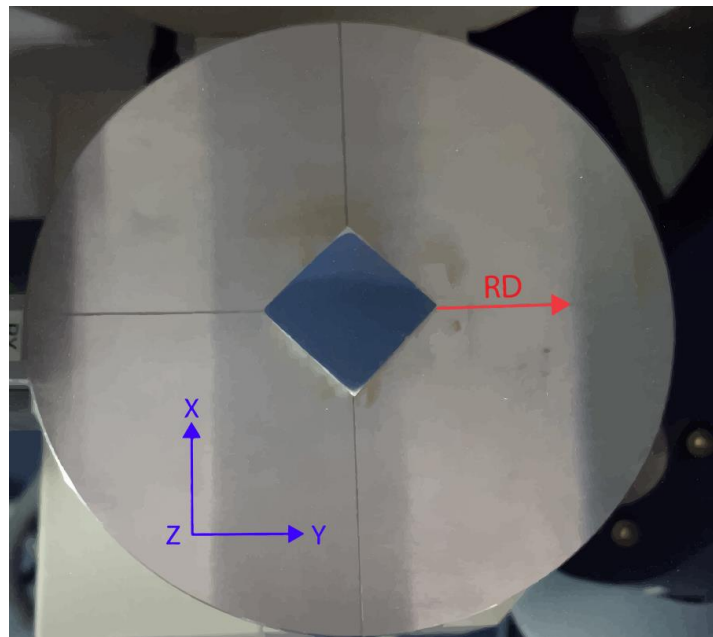


Figure 4. Sample reference system employed on the X-ray measurements. (RD) rolling direction.

Finally, the same samples were used for Electron Backscattering Diffraction (EBSD) images to evaluate the grain refinement of the processed samples. The EBSD analysis was done in a scanning electron microscope JEOL JSM-7001F with a Bruker EBSD detector (15kV). The scanning maps were done with a step size of $1\mu\text{m}$.

3. Results

Some of the deformed specimens used for the Nakazima test are shown in Fig. 5. Fractures were located along the dome apex in most of the samples, indicating that the lubrication system was efficient. As already mentioned, in a typical FLD, there is a minimum point on the major strain, which corresponds to the plane strain condition (FLD_0). This point is often used to evaluating the formability of a metal sheet (Chen et al., 2017). A comparison between the forming limit curve (FLC) obtained from the initial T6 condition and the samples processed after one and two RCS cycles is shown in Fig. 6. A typical profile of a FLC is observed for the initial condition, marked as 6061-T6. However, a continuous decrease of the biaxial ductility as a function of the RCS cycles is observed in the processed specimens, while the FLD_0 has a sudden drop in the one cycle (1C) sample. For the two cycles sample (2C), the value of the FLD_0 was maintained close to the first cycle (1C). The sudden reduction of the forming capacity could be attributed to the high deformation induced by the RCS process. Also, the uneven cross-section characteristic of the process contributes to the localization of the deformation, and thus an earlier fracture could occur.

Table 2 shows the FLD_0 reduction of the aluminum alloys after RCS (present study) and an AA1050 after ARB (Rahmatabadi & Hashemi, 2017). The FLD_0 decreased 42% after the first RCS cycle, while for further cycles the value remained almost constant, the small difference between the values of FLD_0 for 1C and 2C could be due to experimental error. This behavior agrees well with the values obtained for the work hardening coefficient (n) that it is related to the forming capacity of the material. As reported in the literature, the FLD_0 of the AA1050 (Rahmatabadi & Hashemi, 2017) decreased by almost 78% (after one ARB pass). The decrease of the FLD_0 value after one and two RCS cycles was smaller compared to samples with one ARB pass. Nevertheless, it seems that a sudden drop in the FLD_0 value at the beginning of SPD processes is an unavoidable feature, and it might be related to the lack of homogeneity in the microstructure (it is well known that inhomogeneous and UFG microstructures are developed with more RCS and ARB passes (Huang et al., 2004) A comparison between different FLD is a difficult task because

several parameters must be considered, such as strain path, pre-strain condition, the thickness of the sample, and so on. In the study carried out by Rahmatabadi and Hashemi (2017), the AA1050 specimens were annealed, with a thickness of 1 mm, which is similar to the thickness of the present sheets (0.9 mm).

The strain rate sensitivity values were obtained from the data collected from the tensile tests at different temperatures and strain rates. The different strain rate sensitivity coefficients “ m ” at different temperatures for samples undergoing one RCS cycle are shown in Fig. 7. It can be observed relatively high values of “ m ” at the three different tested temperatures compared with the typical values reported for the AA6061 (Chen et al., 2017), although the maximum value obtained for one RCS cycle was 773 K.

On the other hand, the “ m ” values of samples after two RCS cycles (Fig. 8) were still relatively high, showing that as the temperature increases, the “ m ” value decreases; hence, the maximum value was obtained at the lowest tested temperature (573 K). This behavior is inverse to the expected behavior of the strain rate sensitivity observed in non-deformed materials (Chen et al., 2017). The higher values of the “ m ” coefficient in the one cycle (1C) and 2 cycles (2C) conditions could be explained by the grain refinement obtained on the RCS processed samples that are observed in the EBSD maps (see Fig. 9) (Elizalde et al., 2020) and thus a possible activation of different deformation mechanisms, where the grain size plays an important role, such as grain boundary diffusion (Kim et al., 2002; Mohamed et al., 1974).

It is well known that high work hardening (n) and strain rate sensitivity (m) coefficients stabilize the plastic flow of the material. As commonly occurs at room temperature, most of the metals are strain rate-insensible, then just the work hardening coefficient is considered as an indicator of the limit of the stable plastic flow. However, at high-temperature metal forming operations, it is also important to consider the strain rate sensitivity. Hence, considering the results obtained from the FLC at room temperature and the tensile test at different temperatures, the RCS process enhances the forming capacity of the material at high temperature while it is diminished at room temperature.

Fig. 10 presents the ODFs, showing the $\varphi_2 = 45^\circ$, $\varphi_2 = 65^\circ$ and $\varphi_2 = 90^\circ$ sections for the samples at the initial condition (T6) and after one and two RCS cycles. The experimental measurements were carried out by XRD on planes (111), (200), and (220). Table 3 shows the volume fraction calculated for the most common rolling texture components in aluminum alloys. This allows to quantify the texture evolution throughout the RCS process.

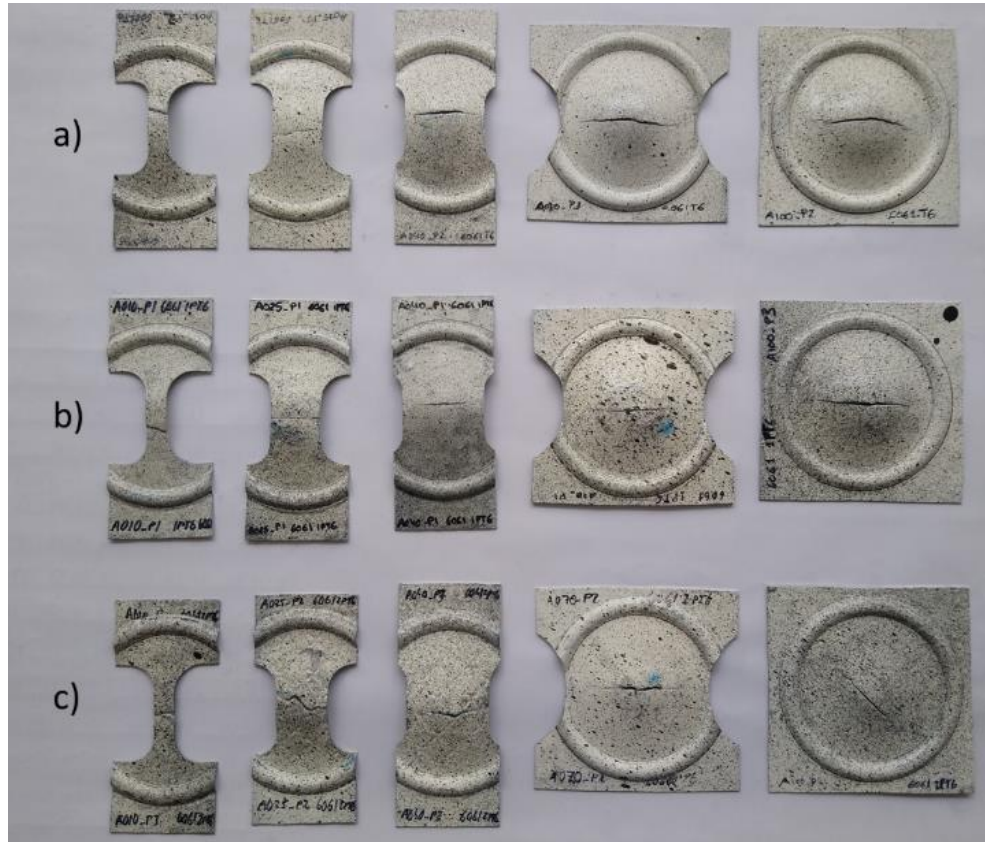


Fig. 5 Samples for a) the initial condition (T6), b) 1C and c)2C, that were tested on the Nakajima test, showing that the fracture occurs on the apex of the dome.

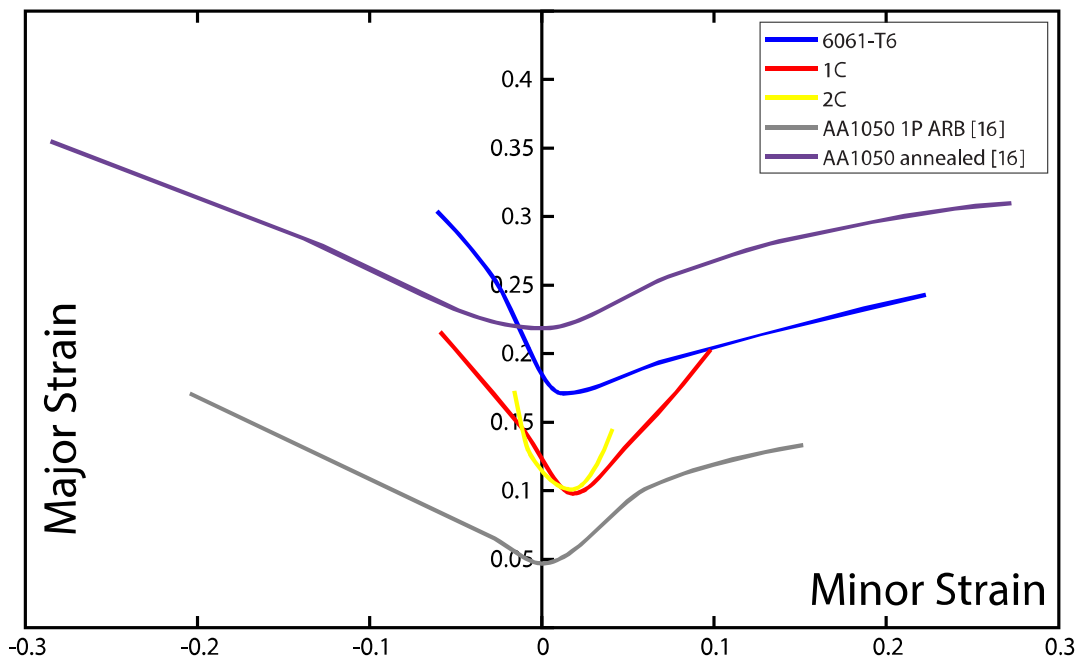


Figure 6. Forming limit curves for the initial 6061-T6 condition and samples processed by RCS and ARB.

Table 2. Comparison of the formability of different aluminum alloys before and after being processed by SPD.

Sample	K [MPa]	n	FLD ₀	variation % of FLD ₀ relative to the initial condition
6061-T6	452.73	0.07	0.171	-
1C	482.90	0.05	0.098	-42%
2C	487.84	0.04	0.101	-41%
AA1050 annealed [16]	-	-	0.23	-
AA1050 1P ARB (Rahmatabadi & Hashemi, 2017)	-	-	0.05	-78%

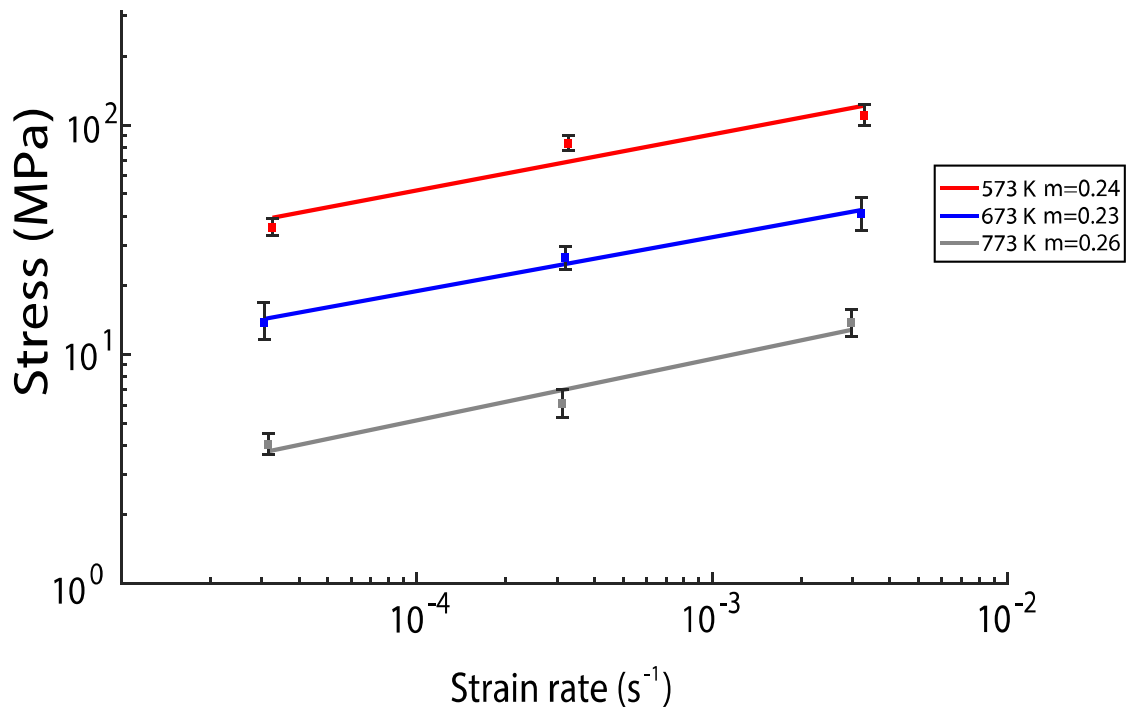


Figure 7. Ultimate stress vs strain rate at different temperatures for samples after one RCS cycle.

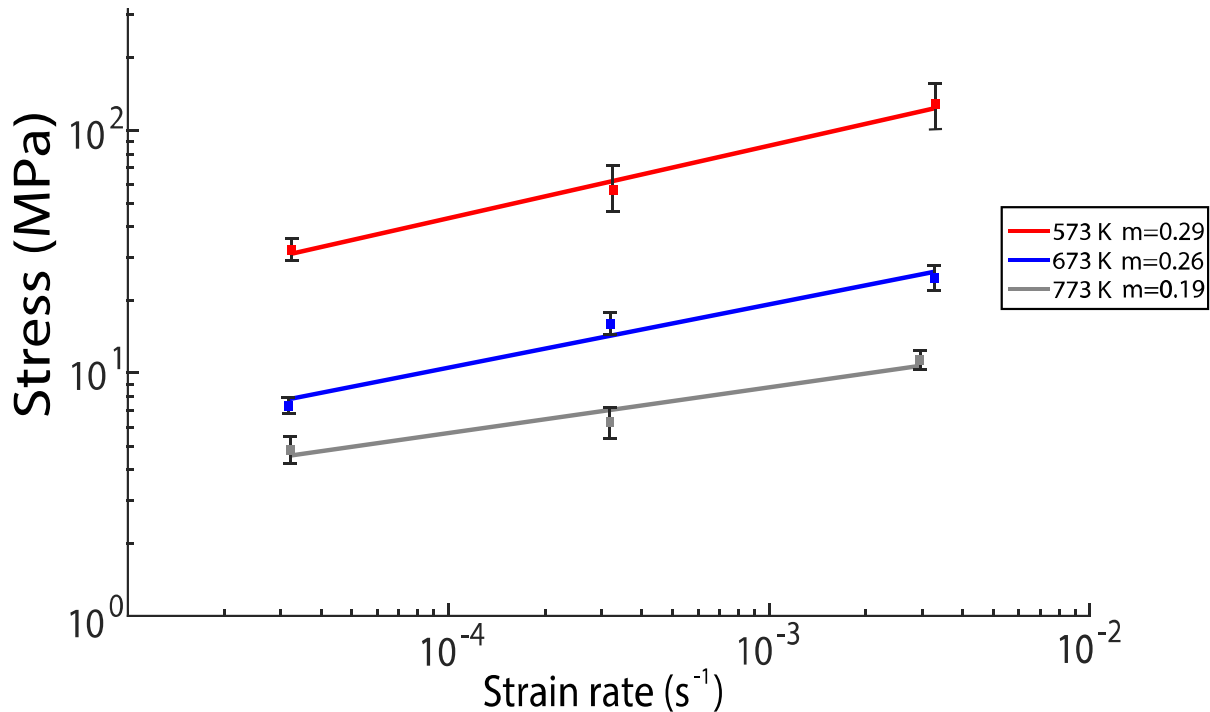


Figure 8. Ultimate stress versus strain rate at different temperatures for samples after two RCS cycles.

The initial condition (T6) clearly shows a strong cube texture that corresponds to the annealed texture for aluminum alloys, agreeing well with the thermomechanical material history. With the RCS cycles, a progressive increment of the S component is observed (marked with a red arrow in Fig. 10). In the case of two RCS cycles, an additional texture component emerged, marked with a black arrow in Fig. 10. The emerging texture component could be related to the bending process that occurs during the RCS process (Muhammad et al., 2017). A significant loss in the intensity of the Cube texture component is also observed, where the volume fraction decreased from 46.95% to 17.81%. According to the literature, this intensity drop could be linked to the rotation of some texture components due to the bending state (Muhammad et al., 2017)

Table 3. Volume fraction of the texture components.

Texture component	T6 (%)	1C (%)	2C (%)
Brass	0.38	1.43	3.77
S	3.10	7.07	12.25
Cu	0.43	0.60	1.34
Cube	46.95	44.06	17.81
S-Cube connecting fiber	9.49	9.97	5.34

It is well known that the texture affects the plastic behavior of the metals (i.e., earing during the deep drawing). Thus, the forming capacity is strongly related and can be controlled by the texture. Also, the presence of cube texture has been related to improving the forming capacity (Engler & Hirsch, 2002; Tóth et al., 1996). So, the weakening of the cube texture component on the RCS processed samples could have affected the forming capacity.

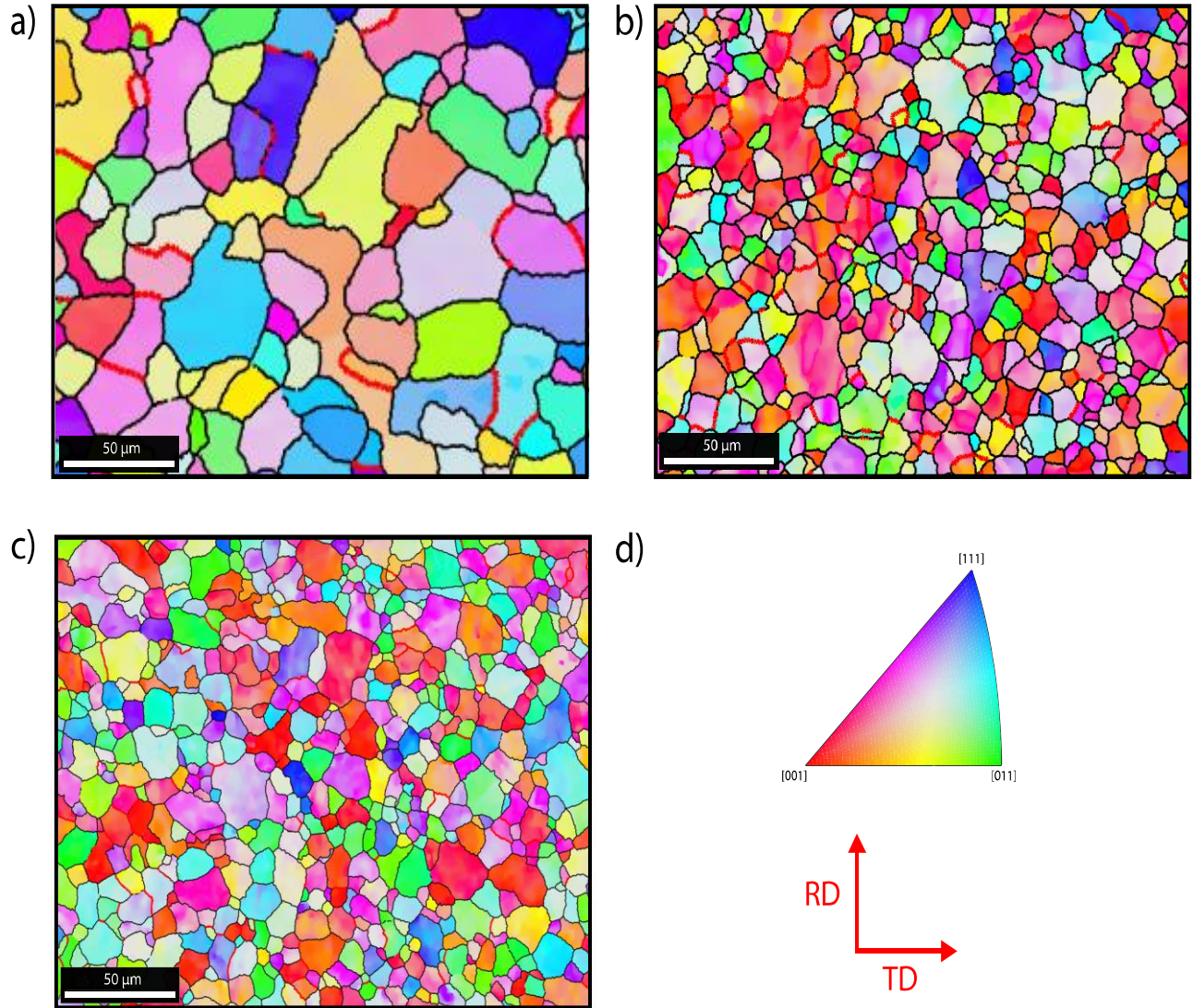


Figure 9. Electron backscatter diffraction (EBSD) orientation maps for a) initial condition; b) one RCS cycle, and c) two RCS cycles; d) Inverse pole figure key and the reference direction.

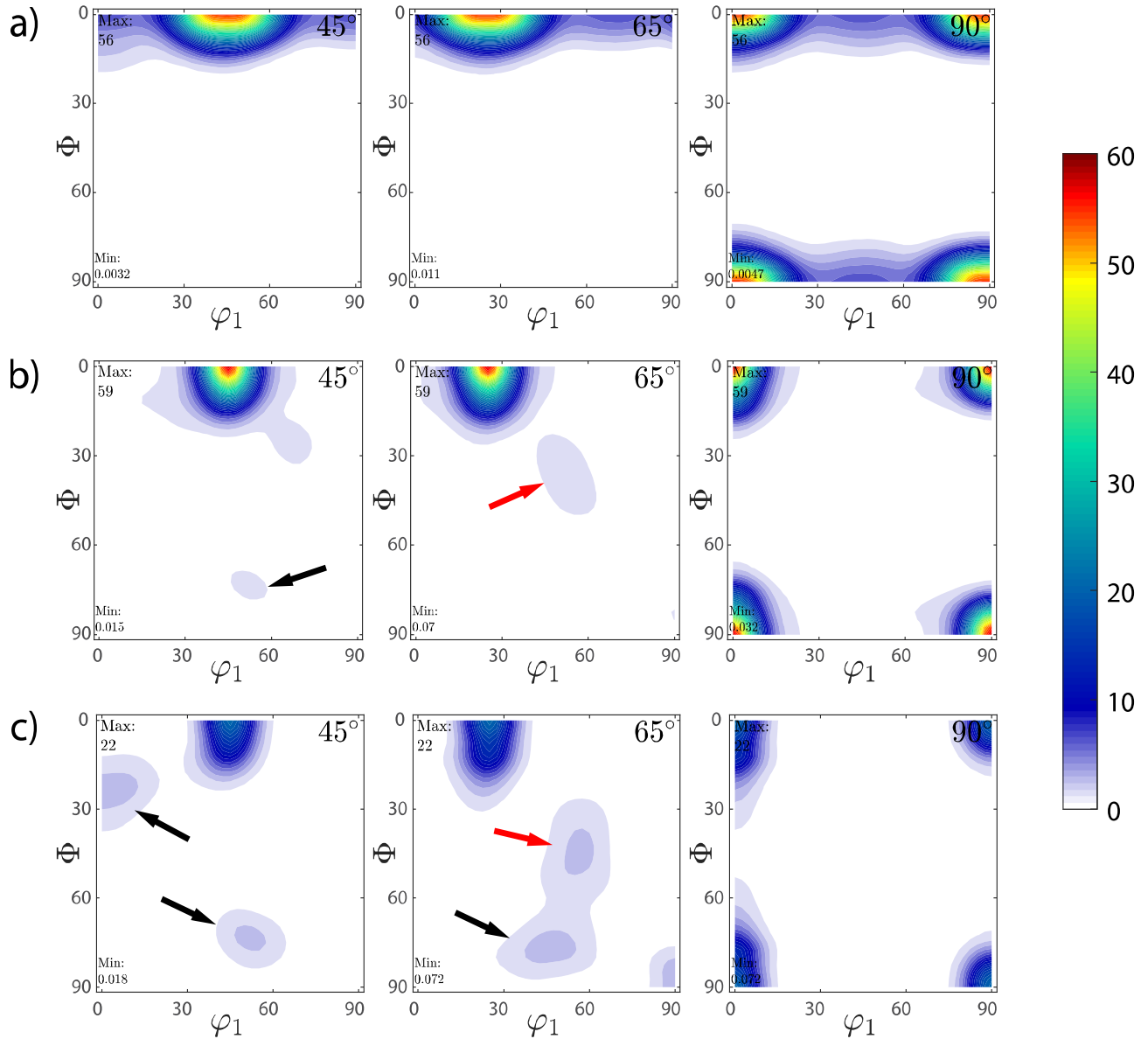


Figure 10. Texture evolution throughout the RCS process represented by the ODF of a) 6061-T6, b) after one RCS cycle, c) after two RCS cycles. (red arrows indicate the S component and black arrows a bending texture component).

4. Conclusions

- The forming limits curves were calculated from Nakazima tests performed in the AA6061-T6 sheets processed with one and two cycles of repetitive corrugation and straightening. The formability decreases in the biaxial condition and a sudden drop of the FLD0 value in the sample after one RCS cycle was observed, followed by a slight increment in the FLD0 value after two RCS cycles.
- The strain rate sensitivity parameter “m” was obtained at different temperatures. The maximum value ($m = 0.29$) was observed at 573 K for the two RCS cycles condition. Contrary to the expected behavior, the “m” value decreased when increasing the testing temperature. This behavior could be attributed to the increase of the grain size due to the high tested temperature.
- A strong cube texture was observed at the initial condition. However, a significant weakening of the cube texture and an increment of the S texture component were also noticed for the RCS processed samples. The loss in the volume fraction of the cube texture component could be related to the reduction in the forming capacity on the RCS processed samples.
- The RCS process shows an enhancement in the forming capacity of the material at high temperatures while it shows a decrement at room temperature. The changes in the formability of the material could be explained by the grain refinement and the development of a combination of different texture components.

Conflict of interest

The authors do not have any type of conflict of interest to declare.

Acknowledgments

The authors acknowledge the funding support from UNAM-DGAPA-PAPIIT- through project IN102321. S.E. acknowledges for the scholarship from CONACyT (No. 450358) and the financial support from PAEP-UNAM. JMC also thanks CONACyT (Mexico) for funding his sabbatical leave at UMSNH. S.E. also acknowledges AGAUR (Generalitat de Catalunya) for his Ph.D. grant. Valuable technical support provided by A. Tejada, E. Hernández, C. Casas, and J. Romero is also acknowledged.

References

- Azushima, A., Kopp, R., Korhonen, A., Yang, D. Y., Micari, F., Lahoti, G. D., Yanagida, A. (2008). Severe plastic deformation (SPD) processes for metals. *CIRP Annals - Manufacturing Technology*, 57(2), 716–735.
<https://doi.org/10.1016/j.cirp.2008.09.005>
- Barlat, F., & Richmond, O. (1987). Prediction of tricomponent plane stress yield surfaces and associated flow and failure behavior of strongly textured f.c.c. polycrystalline sheets. *Materials Science and Engineering*, 95(C), 15–29.
[https://doi.org/10.1016/0025-5416\(87\)90494-0](https://doi.org/10.1016/0025-5416(87)90494-0)
- Bozcheloei, J. E., Sedighi, M., & Hashemi, R. (2019). The effect of temperature on the mechanical properties and forming limit diagram of Al 5083 produced by equal channel angular rolling. *International Journal of Advanced Manufacturing Technology*, 105(10), 4389–4400.
<https://doi.org/10.1007/s00170-019-04586-1>
- Bruder, E. (2019). Formability of Ultrafine Grained Metals Produced by Severe Plastic Deformation – An Overview. *Advanced Engineering Materials*, 21(1), 1–18.
<https://doi.org/10.1002/adem.201800316>
- Chen, Z., Fang, G., & Zhao, J. Q. (2017). Formability Evaluation of Aluminum Alloy 6061-T6 Sheet at Room and Elevated Temperatures. *Journal of Materials Engineering and Performance*, 26(9), 4626–4637.
<https://doi.org/10.1007/s11665-017-2895-0>
- Elizalde, S., Ezequiel, M., Figueroa, I. A., Cabrera, J. M., Braham, C., & Gonzalez, G. (2020). Microstructural evolution and mechanical behavior of an Al-6061 alloy processed by repetitive corrugation and straightening. *Metals*, 10(4).
<https://doi.org/10.3390/met10040489>
- Engler, O., & Hirsch, J. (2002). Texture control by thermomechanical processing of AA6xxx Al-Mg-Si sheet alloys for automotive applications - A Review. *Materials Science and Engineering A*, 336(1–2), 249–262.
[https://doi.org/10.1016/S0921-5093\(01\)01968-2](https://doi.org/10.1016/S0921-5093(01)01968-2)
- Entezami, S., & Honarpisheh, M. (2016). A Study on the Hardness of 7075 and 5052 Aluminum Alloys in the Equal Channel Angular Rolling Process. *Bulletin de La Société Royale Des Sciences de Liège*, 85(1), 879–889.
<https://doi.org/10.25518/0037-9565.5709>

- Ezequiel, M., Elizalde, S., Cabrera, J. M., Picas, J., Figueroa, I. A., Alfonso, I., & Gonzalez, G. (2020). Formability of the 5754-Aluminum alloy deformed by a modified repetitive corrugation and straightening process. *Materials*, 13(3), 1–11. <https://doi.org/10.3390/ma13030633>
- Huang, J., Zhu, Y. T., Alexander, D. J., Liao, X., Lowe, T. C., & Asaro, R. J. (2004). Development of repetitive corrugation and straightening. *Materials Science and Engineering A*, 371(1–2), 35–39. [https://doi.org/10.1016/S0921-5093\(03\)00114-X](https://doi.org/10.1016/S0921-5093(03)00114-X)
- Khamei, A. A., & Dehghani, K. (2015). Effects of strain rate and temperature on hot tensile deformation of severe plastic deformed 6061 aluminum alloy. *Materials Science and Engineering A*, 627, 1–9. <https://doi.org/10.1016/j.msea.2014.12.081>
- Kim, W. J., Kim, J. K., Park, T. Y., Hong, S. I., Kim, D. I., Kim, Y. S., & Lee, J. D. (2002). Enhancement of strength and superplasticity in a 6061 Al alloy processed by equal-channel-angular-pressing. *Metallurgical and Materials Transactions A: Physical Metallurgy and Materials Science*, 33(10), 3155–3164. <https://doi.org/10.1007/s11661-002-0301-4>
- Lapovok, R., Timokhina, I., McKenzie, P. W. J., & O'Donnell, R. (2008). Processing and properties of ultrafine-grain aluminium alloy 6111 sheet. *Journal of Materials Processing Technology*, 200(1–3), 441–450. <https://doi.org/10.1016/j.jmatprotec.2007.08.083>
- Miller, W. S., Zhuang, L., Bottema, J., Wittebrood, A. J., De Smet, P., Haszler, A., & Vieregge, A. (2000). Recent development in aluminium alloys for the automotive industry. *Materials Science and Engineering A*, Vol. 280, pp. 37–49. [https://doi.org/10.1016/S0921-5093\(99\)00653-X](https://doi.org/10.1016/S0921-5093(99)00653-X)
- Mohamed, F. A., & Langdon, T. G. (1974). Deformation mechanism maps based on grain size. *Metallurgical Transactions*, 5(11), 2339–2345. <https://doi.org/10.1007/BF02644014>
- Muhammad, W., Ali, U., Brahme, A. P., Kang, J., Mishra, R. K., & Inal, K. (2017). Experimental analyses and numerical modeling of texture evolution and the development of surface roughness during bending of an extruded aluminum alloy using a multiscale modeling framework. *International Journal of Plasticity*. <https://doi.org/10.1016/j.ijplas.2017.09.013>
- Rahimi, H. R., Sedighi, M., & Hashemi, R. (2018). Forming limit diagrams of fine-grained Al 5083 produced by equal channel angular rolling process. *Proceedings of the Institution of Mechanical Engineers, Part L: Journal of Materials: Design and Applications*, 232(11), 922–930. <https://doi.org/10.1177/1464420716655560>
- Rahmatabadi, D., & Hashemi, R. (2017). Experimental evaluation of forming limit diagram and mechanical properties of nano/ultra-fine grained aluminum strips fabricated by accumulative roll bonding. *International Journal of Materials Research*, 108(12), 1036–1044. <https://doi.org/10.3139/146.111566>
- Ravishankar, C., & Venkadesan, S. (1996). Ductility of sheet metal in the negative minor strain region of forming limit diagrams. *Scripta Materialia*, 35(3), 323–326. [https://doi.org/10.1016/1359-6462\(96\)00138-8](https://doi.org/10.1016/1359-6462(96)00138-8)
- Ratchev P., Van Houtte P., Verlinden B., De Smet P., Neutjens P., Baartman P., Drent P. (1994). Prediction of Forming Limit Diagrams of Al-Mg Rolled Sheets Taking Texture Into Account. *Textures and Microstructures*, 22(C), 219–231. <https://doi.org/10.1155/TSM.22.219>
- Roy, S., Nataraj, B. R., Suwas, S., Kumar, S., & Chattopadhyay, K. (2012). Accumulative roll bonding of aluminum alloys 2219/5086 laminates: Microstructural evolution and tensile properties. *Materials and Design*, 36, 529–539. <https://doi.org/10.1016/j.matdes.2011.11.015>
- Sakai, T., Hamada, S., & Saito, Y. (2001). Improvement of the r-value in 5052 aluminum alloy sheets having through-thickness shear texture by 2-pass single-roll drive unidirectional shear rolling. *Scripta Materialia*, 44(11), 2569–2573. [https://doi.org/10.1016/S1359-6462\(01\)00932-0](https://doi.org/10.1016/S1359-6462(01)00932-0)
- Shin, D. H., Park, J. J., Kim, Y. S., & Park, K. T. (2002). Constrained groove pressing and its application to grain refinement of aluminum. *Materials Science and Engineering A*, 328(1), 98–103. [https://doi.org/10.1016/S0921-5093\(01\)01665-3](https://doi.org/10.1016/S0921-5093(01)01665-3)
- Tóth, L. S., Hirsch, J., & Van Houtte, P. (1996). On the role of texture development in the forming limits of sheet metals. *International Journal of Mechanical Sciences*, 38(10), 1117–1126. [https://doi.org/10.1016/0020-7403\(95\)00110-7](https://doi.org/10.1016/0020-7403(95)00110-7)

Valiev, R. Z., Islamgaliev, R. K., & Alexandrov, I. V. (2000). Bulk nanostructured materials from severe plastic deformation. In *Progress in Materials Science* (45).

[https://doi.org/10.1016/S0079-6425\(99\)00007-9](https://doi.org/10.1016/S0079-6425(99)00007-9)

Yoshida, K., Ishizaka, T., Kuroda, M., & Ikawa, S. (2007). The effects of texture on formability of aluminum alloy sheets. *Acta Materialia*, 55(13), 4499–4506.

<https://doi.org/10.1016/j.actamat.2007.04.014>

Yu, H., Su, L., Lu, C., Tieu, K., Li, H., Li, J., Kong, C. (2016). Enhanced mechanical properties of ARB-processed aluminum alloy 6061 sheets by subsequent asymmetric cryorolling and ageing. *Materials Science and Engineering A*, 674, 256–261.

<https://doi.org/10.1016/j.msea.2016.08.003>